Structures of GMC W 37

Xiao-Liang Zhan, Zhi-Bo Jiang, Zhi-Wei Chen, Miao-Miao Zhang and Chao Song

Purple Mountain Observatory & Key Laboratory for Radio Astronomy, Chinese Academy of Sciences, Nanjing 210008, China; *zbjiang@pmo.ac.cn*

Abstract We carried out observations toward the giant molecular cloud W 37 with the $J = 1-0$ transitions of ^{12}CO, ^{13}CO and $C^{18}O$ using the 13.7 m single-dish telescope at the Delingha station of Purple Mountain Observatory. Based on these CO lines, we calculated the column densities and cloud masses for molecular clouds with radial velocities around $+20\,\mathrm{km\,s^{-1}}$. The gas mass of W 37, calculated from ^{13}CO emission, is $1.7 \times 10^5\,M_\odot$, above the criterion to be considered a giant molecular cloud. The dense ridge of W 37 is a dense filament, which is supercritical in terms of linear mass ratio. Dense clumps found by $C^{18}O$ emission are aligned along the dense ridge at regular intervals of about 2.8 pc, similar to the clump separation caused by large-scale 'sausage instability'. We confirm the identification of the giant molecular filament (GMF) G 18.0–16.8 and find a new giant filament, G 16.5–15.8, located $\sim 0.7°$ to the west of G 18.0–16.8. Both GMFs are not gravitationally bound, as indicated by their low linear mass ratio ($\sim 80\,M_\odot\,\mathrm{pc^{-1}}$). We compared the gas temperature map with the dust temperature map from *Herschel* images, and found similar structures. The spatial distributions of class I objects and the dense clumps are reminiscent of triggered star formation occurring in the northwestern part of W 37, which is close to NGC 6611.

Key words: ISM: clouds – ISM: structure – ISM: kinematics and dynamics – ISM: individual objects (W 37, M 16)

1 INTRODUCTION

Giant molecular clouds (GMCs) are generally accompanied by star formation activities. In the close proximity of the cloud core region of GMC W 37, the well-known star-forming region M 16, also called the 'Eagle nebula', represents the most active area of star formation inside W 37. M 16 is ionized by NGC 6611, a massive young star cluster which is dominated by the massive binary system HD 168076 consisting of an O3.5 V and an O7.5 V star (Evans et al. 2005; Martayan et al. 2008; Alecian et al. 2008). This system has a total of $75 - 80$ solar masses and provides about half the ionizing radiation for the nebula (Evans et al. 2005). Studies of NGC 6611 show that there are some OB members (Martayan et al. 2008; Alecian et al. 2008) and these members are as young as only a few million years (Hillenbrand et al. 1993; Guarcello et al. 2007). The interplay between the open cluster NGC 6611 which has many OB stars and the surrounding molecular clouds (part of W 37) has been observed on various scales. For instance, the CO $1 - 0$ observations with the BIMA interferometer at a resolution of about 0.1 pc targeting the 'pillars of creation' (McLeod et al. 2015) in M 16 show that the velocity gradients along the 'pillars of creation' are produced from impact by an ionization front interacting with a cloud core (Pound 1998). On the scale of the whole GMC

W 37, *Herschel* images enable Hill et al. (2012) to find a prominent eastern filament running southeast-northwest and away from the high-mass star-forming central region M 16 and the cluster NGC 6611, as well as a northern filament which extends around and away from the cluster in the forms of dust temperature and column density maps. Moreover, the dust temperature in each of these filaments decreases with increasing distance from the cluster NGC 6611, indicating a heating penetration depth of $\sim 10\,\mathrm{pc}$ in each direction in $3 - 6 \times 10^{22}\,\mathrm{cm^{-2}}$ column density filaments. These results suggest that the cluster NGC 6611 impacts the temperature of future star-forming sites inside the W 37 cloud, modifying the initial conditions of collapse (Hill et al. 2012).

Previous CO line observations toward the GMC W 37 are from a $^{12}CO\,1 - 0$ survey of the entire Milky Way (Dame et al. 2001). This CO survey (hereafter 1.2 m CO survey) has an angular resolution of $\sim 8.5'$ at 115 GHz, and a velocity resolution mostly around 0.65 km s^{-1}. Along the same line of sight (LOS) toward W 37, the 1.2 m CO survey detects CO line emissions in the range between $-5\,\mathrm{km\,s^{-1}}$ and $140\,\mathrm{km\,s^{-1}}$. Ragan et al. (2014) identify a giant molecular filament (GMF), which is running in the Galactic longitude range $18.0° - 16.8°$ with a length of 88 pc and its near end is located only about $15'$ away from the GMC W 37. The velocity range of this GMF is

$21 - 25\,\mathrm{km\,s^{-1}}$ in the form of $^{13}\mathrm{CO}\,1-0$ line emissions, very close to the velocity of W 37 ($\sim 20\,\mathrm{km\,s^{-1}}$). Because of this coherent velocity structure, Ragan et al. (2014) regard this GMF as being associated with W 37.

In this work, we present the preliminary results of the CO $1-0$ line observations toward the Galactic coordinate range $l = 15.5 - 18.5°$ and $b = 0.0 - 1.5°$, as part of the new Galactic plane survey using the $J = 1 - 0$ transitions of $^{12}\mathrm{CO}$, $^{13}\mathrm{CO}$ and $\mathrm{C^{18}O}$ molecules. In Section 2, the observations and data reduction are described. The results based on the CO lines are presented in Section 3. Section 4 discusses the structures of W 37. A summary is provided in Section 5.

2 OBSERVATIONS AND DATA REDUCTION

We observed GMC W 37 in $^{12}\mathrm{CO}\,1-0$, $^{13}\mathrm{CO}\,1-0$ and $\mathrm{C^{18}O}\,1-0$ with the Purple Mountain Observatory Delingha (PMODLH) 13.7 m telescope (Zuo et al. 2011) as one of the scientific target regions of the Milky Way Imaging Scroll Painting (MWISP) project[1] (Sun et al. 2015). The time span of the observations is from 2013 October 6 to December 13. The three CO $1-0$ lines were observed simultaneously with the 9-beam Superconducting Spectroscopic Array Receiver (Shan et al. 2012) working in sideband separation mode and with the Fast Fourier transform spectrometer. The pointing accuracy is checked every year by carrying out five-point observations of planets (e.g., Jupiter), and it is found to be stably better than $5''$ when tracking targets. During all observations, standard sources were observed every two hours for calibration and monitoring the systematic performance. The typical receiver noise temperature (T_{rx}) is about 30 K as given by the status report of PMODLH in 2013. The typical system temperature during observations is 280 K for $^{12}\mathrm{CO}\,1-0$ and 185 K for $^{13}\mathrm{CO}\,1-0$ and $\mathrm{C^{18}O}\,1-0$.

Our observations covered an area from Galactic longitude $15.5°$ to $18.5°$ and Galactic latitude from $0.0°$ to $1.5°$ (see Fig. 1). The GMC W 37 was mapped using the on-the-fly observing mode, with the standard chopper wheel method used for calibration (Penzias & Burrus 1973). To conduct the observation, the whole region is split into many cells, each with a dimension of $30' \times 30'$. Each cell is scanned along the Galactic longitude and latitude direction on the sky at a constant rate of $50''$ per second, and the receiver records spectra every 0.3 second. Every cell was repeatedly observed with this observation pattern until the root mean square (RMS) of spectra decreased down to the RMS levels required by MWISP, which are 0.5 K for the $^{12}\mathrm{CO}\,1-0$ line and 0.3 K for both the $^{13}\mathrm{CO}\,1-0$ and $\mathrm{C^{18}O}\,1-0$ lines.

After removing the bad channels in the spectra, we calibrated the antenna temperature (T_a^*) to the main beam temperature (T_{mb}) with a main beam efficiency of 44%

for $^{12}\mathrm{CO}$ and 48% for $^{13}\mathrm{CO}$ and $\mathrm{C^{18}O}$. The calibrated data were then re-gridded to $30''$ pixels and mosaicked to a FITS cube using the GILDAS software package (Guilloteau & Lucas 2000). A first order baseline was applied to the spectra. The resulting RMS level is 0.55 K for $^{12}\mathrm{CO}$ at the resolution of $0.159\,\mathrm{km\,s^{-1}}$, and 0.25 K for $^{13}\mathrm{CO}$ and 0.22 K for $\mathrm{C^{18}O}$ at the resolution of $0.166\,\mathrm{km\,s^{-1}}$. A summary of the observational parameters is provided in Table 1.

3 RESULTS

3.1 The Basic Characteristics of the CO Emissions

The average spectra of the whole observed region in the three lines are shown in Figure 2. We clearly see several velocity components in the range $0 - 140\,\mathrm{km\,s^{-1}}$ in the $^{12}\mathrm{CO}\,1-0$ spectrum; among them the component at around $20\,\mathrm{km\,s^{-1}}$ is strongest. Another component slightly weaker than the $20\,\mathrm{km\,s^{-1}}$ component shows a radial velocity at around $24\,\mathrm{km\,s^{-1}}$. Other velocity components are significantly weaker than the components of $20\,\mathrm{km\,s^{-1}}$ and $24\,\mathrm{km\,s^{-1}}$. Those diverse velocity components likely come from different molecular clouds with different distances along the same LOS. Given the distances of the Galactic spiral arms from the Sun (Vallée 2008), as well as the rotation curve of the Galaxy (Mannheim & O'Brien 2012), we can attribute most of the observed CO emissions to their natal spiral arms. The components of W 37 which are peaked at $20\,\mathrm{km\,s^{-1}}$ and $24\,\mathrm{km\,s^{-1}}$ have kinematic distances between $2.0 - 2.4\,\mathrm{kpc}$. Because of the association between M 16 and W 37, the distance of M 16, $2.0\,\mathrm{kpc}$, used by Linsky et al. (2007) is accepted here for W 37's distance. W 37 is located on the near side of the Sagittarius arm. We can marginally identify the molecular clouds located on the far side of the Sagittarius arm, which have a typical radial velocity in the range $60 - 70\,\mathrm{km\,s^{-1}}$, as seen in Figure 3. The third strongest component around $50\,\mathrm{km\,s^{-1}}$ is probably located in the Scutum-Centaurus Arm. Besides these molecular clouds in the spiral arms, there are other molecular clouds with radial velocities which cannot be attributed to any spiral arms lying along the same LOS. They might be inter-arm molecular clouds with relatively low density.

3.2 The Structure of W 37

This paper focuses on the bulk gas component of W 37 with a peak radial velocity of $\sim 20\,\mathrm{km\,s^{-1}}$.

Figure 1 shows the integrated intensity maps of the three lines. The distribution of $^{12}\mathrm{CO}$ gas outlines the overall morphology of the GMC W 37, which is running perpendicularly to the Galactic plane with a length of about 46 pc, while the $^{13}\mathrm{CO}\,1-0$ emissions trace the relatively dense parts of W 37, which are also distributed perpendicularly to the Galactic plane. In the $\mathrm{C^{18}O}\,1-0$ emis-
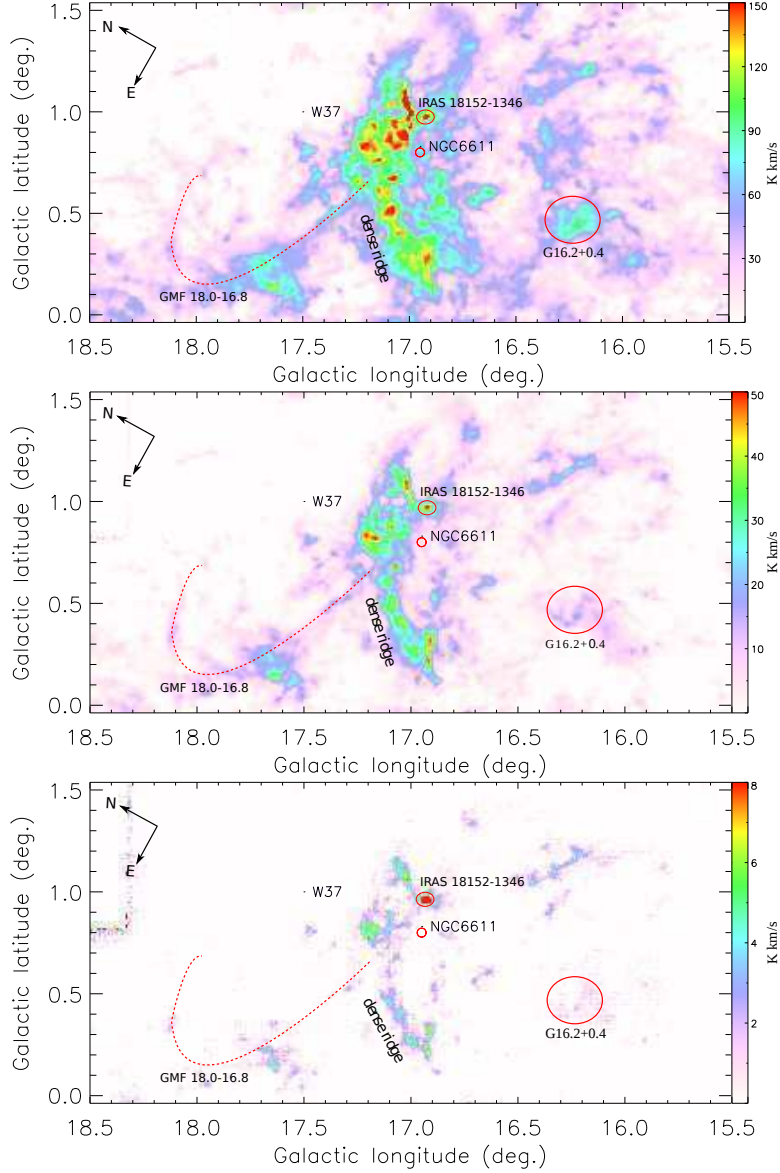

Fig. 1 *Top panel*: the integrated intensity map of ^{12}CO $1 - 0$ in the range $16 - 27$ km s^{-1}; *middle*: same as the top but for ^{13}CO $1 - 0$; *bottom*: same as the top but for C^{18}O $1 - 0$. The large-scale filament G 18.0–16.8 is outlined by the red dashed line. The locations of the high-mass young cluster NGC 6611, IRAS 18152–1346 and isolated molecular cloud G16.2+0.4 are denoted by the red circles/ellipses.

Table 1 Observational Parameters

Line $(J = 1 - 0)$	v_0 (GHz)	HPBW ($''$)	T_{sys} (K)	η_{mb}	δ_v (km s^{-1})	T_{mb} RMS noise (K)
^{12}CO	115.271204	52±3	220–500	43.6%	0.160	0.55
^{13}CO	110.201353	52±3	150–310	48.0%	0.158	0.22
C^{18}O	109.782183	52±3	150–310	48.0%	0.158	0.22

Notes: The beam width and main beam efficiency are given by the annual report about the telescope status in 2013.

sion, W 37 can be split into two major parts: the dense filamentary structure in between $b = 0.2 - 0.7°$ (hereafter the dense ridge) and the northwestern part closest to the massive cluster NGC 6611. A very bright clump located in the northwest of NGC 6611 shows stronger C^{18}O emission than the dense ridge. Indebetouw et al. (2007) identified this bright clump as a massive young stellar object (YSO), also known as IRAS 18152–1346.

The column density map of W 37 (with $37''$ resolution, see fig. 2 in Hill et al. 2012) derived from *Herschel*
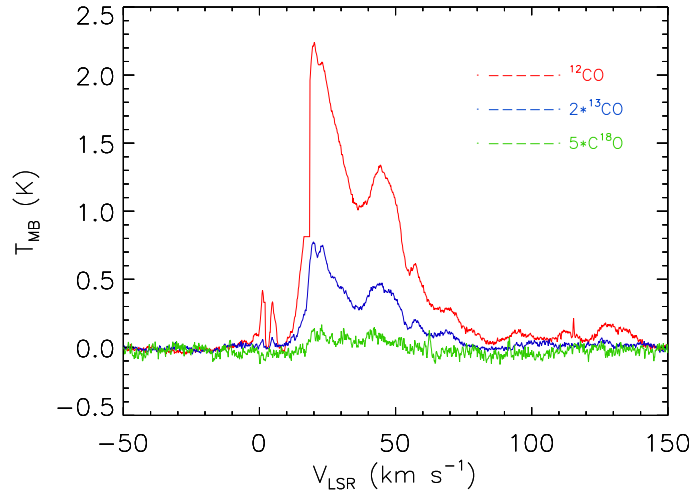
Fig. 2 Average spectra of the ^{12}CO 1−0, ^{13}CO 1−0 and C^{18}O 1−0 lines in the observed region.
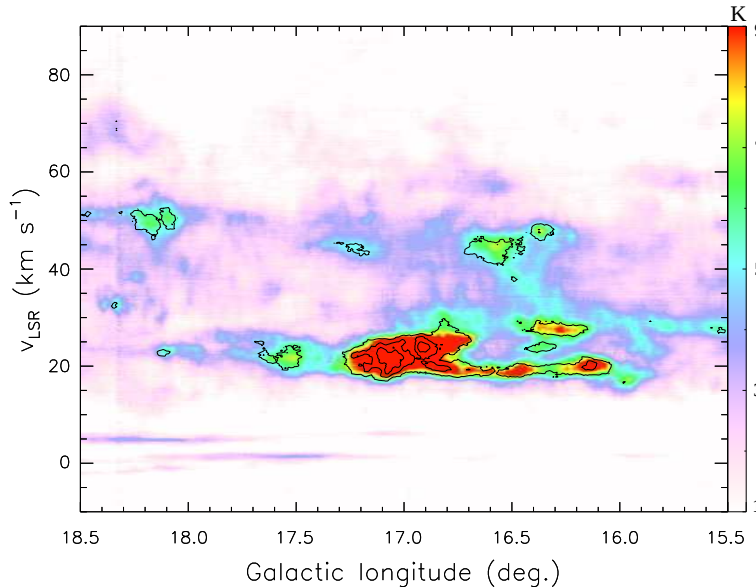

Fig. 3 Position-velocity map of ^{12}CO 1−0 emission in intensity (*color scale*) and ^{13}CO 1−0 emission in contours (*black*). The contours start from 1 K with an interval of 1 K. The CO emissions with radial velocities greater than 90 km s^{-1} are not shown because of their weaknesses.

images shows very similar morphology with the ^{12}CO gas distribution. However, what the dust column density map cannot tell us is the morphology variation of W 37 along with the radial velocity in our CO line observations. Therefore, we show this morphological variation in the form of a ^{13}CO 1 − 0 channel map in Figure 4. The dense ridge appears mainly in the range ∼ 20−23 km s^{-1}, while the northwestern part shows a wider velocity range from 17 km s^{-1} to 24 km s^{-1}. There are dense clumps ($V_{LSR} \gtrsim 25$ km s^{-1}) at positions around $l = 16.2°$ and $b = 0.4°$, separated from the dense ridge by about 0.7°, or 25 pc at a distance of 2.0 kpc. We refer to these dense clumps as the isolated molecular cloud G16.2+0.4, which is independent of GMC W 37.

Interestingly, we note a pair of filaments located on the two sides of W 37 in the velocity range $20 - 23$ km s^{-1}. This pair of filaments is symmetric with respect to W 37. The position–velocity maps of this symmetric pair of filaments are shown in Figure 5. This pair of filaments shows a coherent velocity distribution that is peaked for both at around 23 km s^{-1}.

3.3 Masses and Column Densities of the Clouds

Better than the 1.2 m CO survey using a single CO line, our new CO three-line survey enables us to obtain the column density of CO gas under the assumption of local thermodynamic equilibrium (LTE). In general, the ^{12}CO 1 − 0 line
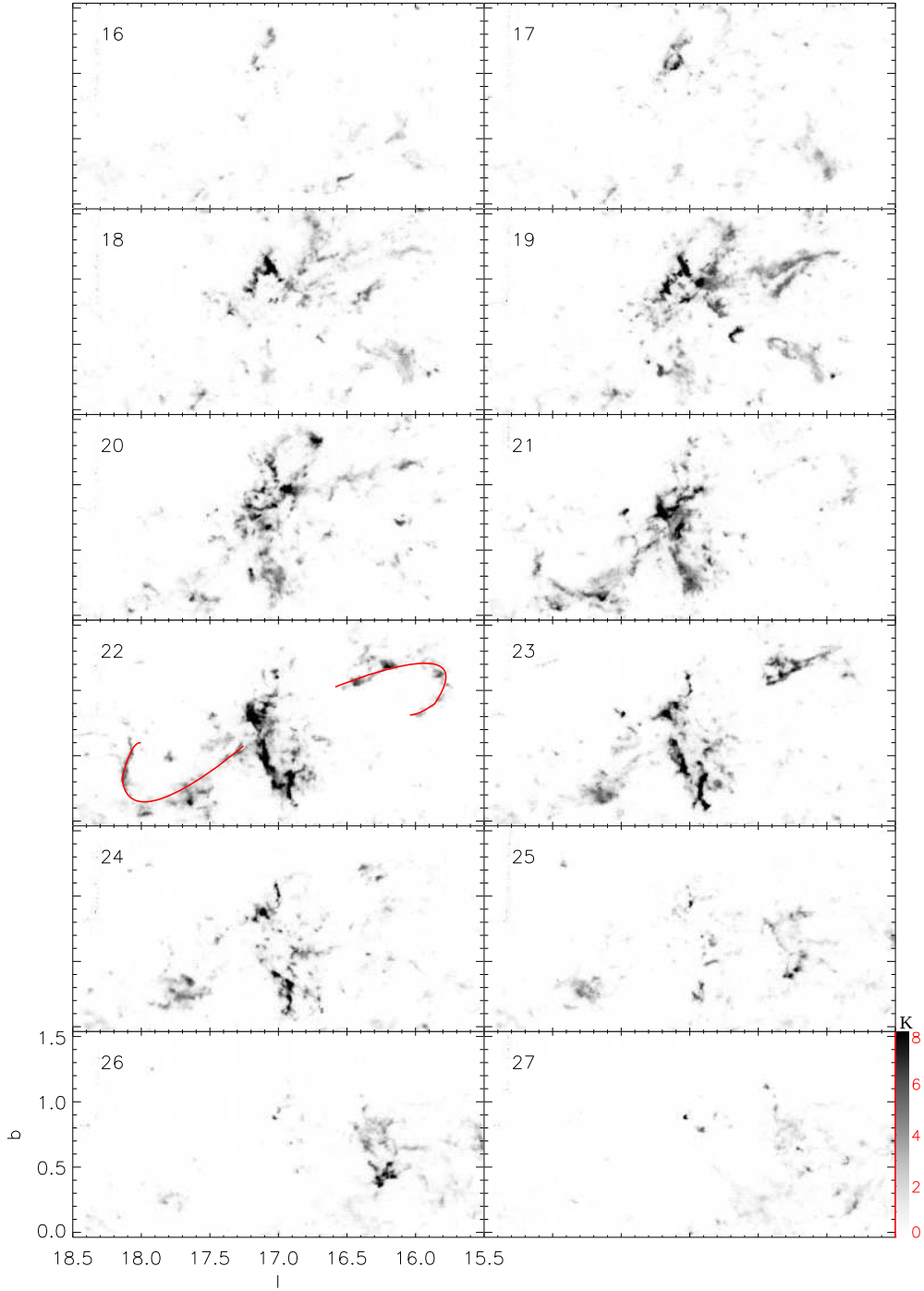
Fig. 4 Channel map of ^{13}CO $1 - 0$ emission for the observed region. Each frame is marked with the corresponding central velocity in km s^{-1} on the upper-left corner. In the 22 km s^{-1} frame, the sketched curves in red identify the pair of filaments.

is optically thick, hence the excitation temperature can be determined via the formula

$$T_{\text{ex}} = 5.5 / \ln\left(1 + \frac{5.5}{T_{\text{B}}(^{12}\text{CO}) + 0.82}\right). \quad (1)$$

We assume that ^{13}CO and C^{18}O have the same T_{ex} as ^{12}CO. Supposing that the ^{13}CO and C^{18}O lines are optically thin, the optical depths of the two isotopes of ^{12}CO

are only functions of T_{B} and T_{ex}

$$\tau_0 = -\ln\left[1 - \frac{T_{\text{B}}}{5.3}\left\{\left[\exp\left(\frac{5.3}{T_{\text{ex}}} - 1\right)\right]^{-1} - 0.16\right\}^{-1}\right]. \quad (2)$$

To obtain the column density for a molecule, i.e. ^{13}CO or C^{18}O, one must sum over all energy levels of the molecule. In the LTE case, the total column density of ^{13}CO or C^{18}O
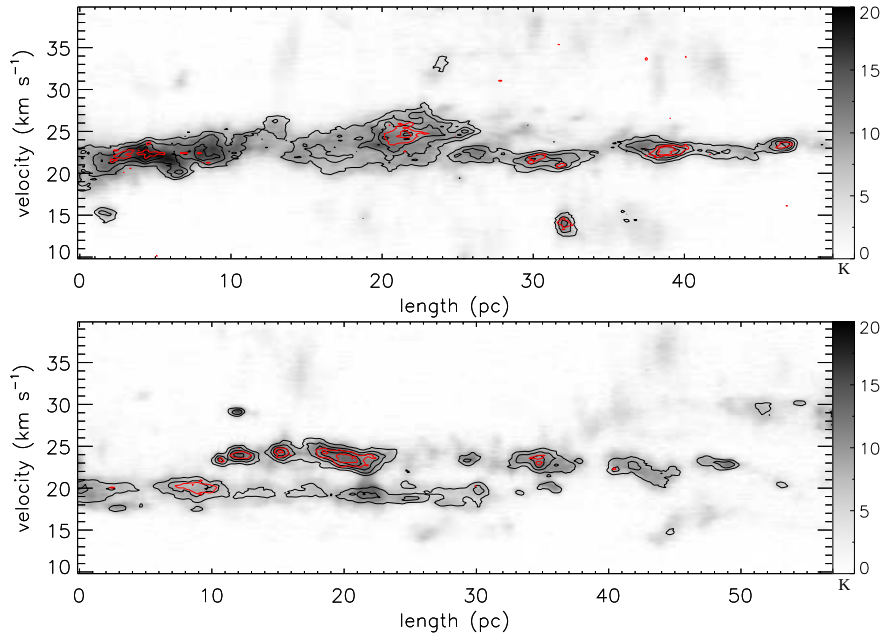
Fig. 5 Position-velocity maps of ^{12}CO 1−0 emission in intensity (grey scale) of the two GMFs, along the paths sketched by the red curves in Fig. 4. The overlaid black contours are ^{13}CO 1 − 0 emission starting from 1.3 K with an interval of 1.3 K, and red contours are ^{18}CO 1 − 0 emission starting from 0.8 K with an interval of 0.4 K. The left part is shown in the top panel, and the right part in the bottom panel. In each panel, the length of each filament is counted from the end toward the side of W 37.
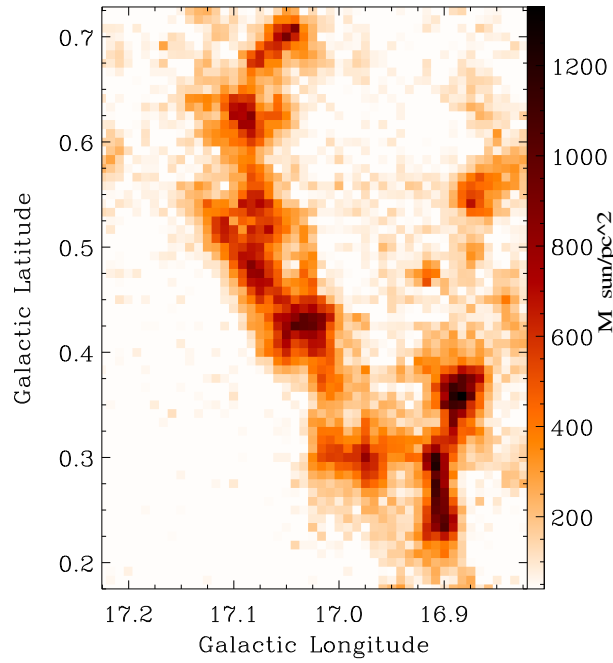

Fig. 6 Surface mass density map calculated from the C^{18}O 1−0 line emission for the dense ridge of W 37.

is given by

$$N(\text{total})_{\text{CO}} = 3.0 \times 10^{14} \frac{T_{\text{ex}} \int \tau(v) \mathrm{d}v}{1 - \exp\{-5.3/T_{\text{ex}}\}}. \quad (3)$$

Substituting $\tau(^{13}\text{CO})$ and $\tau(\text{C}^{18}\text{O})$, one can calculate the column density of ^{13}CO and C^{18}O, respectively.

Adopting fractional abundances of H$_2$/^{13}CO= 7×10^5 and H$_2$/C^{18}O= 7×10^6 (Castets & Langer 1995), $N(^{13}\text{CO})$ and $N(\text{C}^{18}\text{O})$ are then converted to the corresponding H$_2$ column densities. Then we calculate the mass of the H$_2$ gas as

$$M_{\text{LTE}} = \mu m_{\text{H}} N(\text{H}_2) S, \quad (4)$$

where $\mu = 2.83$ is the average molecular weight, and S is the summed area of $^{13}CO\,1 - 0$ with signal to noise ratios > 3. Note that this criterion filters out many diffuse areas where only the ^{12}CO lines are significant. Therefore, the total masses of the molecular clouds calculated from the $^{13}CO\,1 - 0$ line can be treated as lower limits. Specifically, we refer to the molecular gas mass derived from the $C^{18}O\,1 - 0$ line as the dense gas mass because of the highest critical density of the $C^{18}O$ molecule. The physical properties of the GMC W 37 and the isolated cloud G16.2+0.4 are listed in Table 2. W 37's physical properties and length (46 pc) all fall in typical ranges for the GMCs previously identified (e.g., Murray 2011 and references therein). The comparison between W 37 and G16.2+0.4 clearly demonstrates the physical differences between a GMC and a molecular cloud.

4 DISCUSSION

4.1 Filamentary Structures

The dense ridge exhibits a filament morphology between $b \approx 0.25 - 0.72$. We display this peculiar part in Figure 6 in order to highlight its properties. The dense ridge is clumpy, and clumps are distributed along the filament. The clumpy structure is most likely the result of gravitational collapse of a cylinder. If we regard the dense gas traced by the $C^{18}O\,1-0$ emission as a whole, the stability of the filament can be described by the virial parameter $\alpha = M_{vir}/M = 2\sigma_v^2 l/GM$ (Su et al. 2015 and references therein), where $\sigma_v = \Delta_{C^{18}O}/2.355$, l and G are the average velocity dispersion of $C^{18}O\,1 - 0$ emission, the length of the dense filament and the gravitational constant, respectively. In the calculation, we regard the long dense filament as a symmetrical cylinder. The geometric size of the cylinder ($\sim 18\,\mathrm{pc} \times 2\,\mathrm{pc} \times 2\,\mathrm{pc}$) can be obtained from the $C^{18}O\,1-0$ surface mass density map ($\sim 216\ M_\odot\ \mathrm{pc}^{-2}$ cutoff in Fig. 6). We use the mean full width at half maximum (FWHM) of $C^{18}O\,1 - 0$ emission ($\Delta_{C^{18}O} = 1.9\,\mathrm{km\,s}^{-1}$) in the filament to estimate the mean velocity dispersion $\sigma_v = 0.8\,\mathrm{km\,s}^{-1}$. The virial parameter α is estimated to be 0.6, indicating that the dense filament is gravitationally bound. Moreover, we can estimate the fragmentation separation within the filament to clarify whether 'sausage instability' dominates the fragmentation process. Adopting $10^4\,\mathrm{cm}^{-3}$ as the mean density of the dense filament, the filament scale height $H = \sigma_v(4G\pi\rho_c)^{-0.5}$ is about 0.14 pc due to the 'sausage instability' of a self-gravitating fluid cylinder (Su et al. 2015 and references therein). This leads to a spacing of $22\,H \sim 3\,\mathrm{pc}$ between the fragmentating clumps. Applying the clump identification algorithm 'GaussClumps' integrated in the Starlink/CUPID package[2] to the surface mass density map of $C^{18}O\,1 - 0$ emission, seven clumps are found along the dense filament. The

---

[2] For more information about CUPID see *http://starlink.eao.hawaii. edu/starlink/CUPID*

seven clumps are roughly regularly spaced with a mean fragmentation separation of about 2.8 pc, which results in good agreement with the 'sausage instability' model. We notice another shorter and denser filament running along $b = 0.2 - 0.4°$ in the right lower corner of Figure 6, which is worthy of detailed analyses in a separate paper.

We recall the pair of filaments almost perpendicular to W 37, that are apparent in the ^{13}CO channel map in Figure 4. The left part was identified by Ragan et al. (2014) as a GMF named G 18.0–16.8. However, our CO data reveal the counterpart of G 18.0–16.8, which is not found in Ragan et al. (2014). In view of the coherent velocity distribution of this pair of filaments, the GMF found by Ragan et al. (2014) is only one part of this pair. Although the two parts of this pair are continuous in velocity, they are separated by a gap of about 28 pc, where W 37 is located in between. The right half (hereafter G 16.5–15.8) has a length of about 50 pc, at a distance of 2 kpc. Moreover, the two GMFs have total masses on the order of $10^4\ M_\odot$, which are comparable to the masses of GMFs reported by Wang et al. (2015). Ragan et al. (2014) associate the left GMF with GMC 37 upon considering the comparable radial velocities between them. Because of the same argument, we regard G 16.5–15.8 as being associated with W 37.

The two GMFs are separated by W 37. This might be the result of dynamical evolution of a whole GMF, which is disconnected by the contraction of W 37 located in its middle. In addition, about six class I objects have positions that overlap G 18.0–16.8, but no class I object is lying on G 16.5–15.8 (see Fig. 8). However, this differential distribution between the two GMFs is not noticed for the class II objects, which seem to be uniformly distributed along the two GMFs. The different distributions of class I objects along the two GMFs could be simply due to their different physical properties. We can estimate the linear mass density (mass per unit length) of the two GMFs, which could help to clarify whether they are gravitationally stable or not. The mean linear mass density is thus estimated to be $88\ M_\odot\ \mathrm{pc}^{-1}$ and $73\ M_\odot\ \mathrm{pc}^{-1}$ for the left and right GMF, respectively, where gas mass is calculated from the $^{13}CO\,1 - 0$ emission, filament length is obtained from Figure 5, and mean filament width is derived by dividing the filament area by filament length. The linear mass density has a maximum value of $M_{vir}/l = 465(\frac{\sigma}{\mathrm{km\,s}^{-1}})^2\ M_\odot\ \mathrm{pc}^{-1}$, over which a filament will break up into pieces. The mean FWHM of $^{13}CO\,1 - 0$ emission (see Table 3) leads to a maximum linear mass density of about $300\ M_\odot\ \mathrm{pc}^{-1}$ for the two GMFs. Both GMFs are not dense enough to initiate large-scale fragmentation.

On the other hand, the mean dense gas fractions $M_{C^{18}O}/M_{^{13}CO}$ of the two GMFs are similar, which are 0.48 and 0.46 for the left and right GMF, respectively. To conclude, the mean physical properties of the two GMFs are very similar (see also Table 3), which contradicts the different distributions of class I objects. Alternatively, a

Table 2 Physical Properties of the Molecular Clouds

Cloud	Velocity range [km s^{-1}]	$N(H_2)$ ^{13}CO$(1-0)$ [cm^{-2}]	$N(H_2)$ C^{18}O$(1-0)$ [cm^{-2}]	Cloud mass [$M_\odot$]	Dense Gas mass [$M_\odot$]
W 37	$17-25$	1.1×10^{22}	2.1×10^{22}	1.7×10^5	1.0×10^5
G16.2+0.4	$25-27$	1.4×10^{21}	4.4×10^{21}	2.4×10^3	3.4×10^2

Notes: For both molecular clouds, mass calculation is made at a distance of 2.0 kpc (Linsky et al. 2007).

Table 3 Properties of GMFs

Transition Line	Mass ($10^4 \, M_\odot$)		$N(H_2)$ (10^{21} cm^{-2})		Δv (km s^{-1})	
	right	left	right	left	right	left
^{13}CO$(1-0)$	1.2	2.7	3.1	3.8	1.9	2.0
C^{18}O$(1-0)$	0.55	1.3	4.7	5.6	1.4	1.2

Notes: For both molecular clouds, mass calculation is made at a distance of 2.0 kpc (Linsky et al. 2007).

more plausible explanation is that class I objects just overlap the left GMF along the same LOS and there is no physical association.

4.2 Young Stellar Objects in W 37

Figure 7 shows the excitation temperature map of GMC W 37. There are two domains of $T_{ex} \gtrsim 30$, which correspond to the dense ridge and the northwestern part of W 37, respectively. These relatively warm clouds are believed to be at the very beginning phases of gravitational contraction. Moreover, the dense ridge and the northwestern part of W 37 are also prominent in the dust temperature map from *Herschel* images (Hill et al. 2012), whereas, they both show dust temperatures of about 17 K, which is lower than the gas temperature. This temperature difference might naturally come from the two temperature tracers. The detected ^{12}CO $1 - 0$ emission mostly originates from the surface layer because emission from the inner areas are self-absorbed, however, the dust continuum emission even from the innermost area can also be detected. In addition, this temperature difference is consistent with the theoretical point that the surface layer is warmer than the inner area of a molecular cloud.

We used the latest Wide-field Infrared Survey Explorer (WISE) (Wright et al. 2010) source catalog AllWISE[3] to identify YSO candidates located inside the observed region, adopting the criteria from Koenig & Smolin (2014) The class I objects are mostly distributed in the proximity of molecular gas, but the class II objects can also be frequently seen in areas with little/no molecular gas (see Fig. 8). This phenomenon can be interpreted as the result of the age differences between class I and class II objects. Furthermore, class I objects are better tracers of early stage star formation than class II objects. We still note that the class II objects have a trend of being concentrated toward the GMC W 37, and many more class I objects are found in the northwestern part than in the dense

---

[3] The AllWISE catalog can be retrieved from *http://wise2.ipac. caltech.edu/docs/release/allwise/*

ridge. The class I objects in the northwestern part of W 37 are located close to NGC 6611. Hill et al. (2012) argued that NGC 6611 impacts the conditions of W 37 by heating. The penetration depth of this heating effect is found to be about 9 pc for the northwestern part whose column density is 2.3×10^{22} cm^{-2} (Hill et al. 2012). This penetration depth is almost identical to the northwestern part's size, indicating that molecular clumps inside the northwestern part are very likely influenced by the cluster's heating effect. More class I objects found in the area close to NGC 6611 can be interpreted as being the result of the heating effect of the cluster, i.e., NGC 6611 triggers star formation in the northwestern part of W 37. Because the northwestern part of W 37 is massive and dense enough to avoid being destroyed by the high-mass cluster NGC 6611, star formation inside this area can be the result of the direct compression of pre-existing density enhancements in this area (Elmegreen 1998). Therefore, the northwestern part of W 37 is a promising candidate for triggering star formation by effects from the cluster, and is worthy of continuous investigation.

5 SUMMARY

We observed the $J = 1 - 0$ transition lines of ^{12}CO, ^{13}CO and C^{18}O toward GMC W 37, as part of the MWISP project. The bulk of W 37's molecular gas has radial velocities between $17 - 24$ km s^{-1}, which can be attributed to the near end of the Sagittarius arm. The gas mass traced by ^{13}CO emission is $1.7 \times 10^5 \, M_\odot$ for W 37. The dense ridge of W 37 is a dense and gravitationally bound filament, as indicated by its large linear mass ratio. Dense clumps traced by C^{18}O emission are regularly spaced along the dense ridge with a mean separation of about 0.28 pc, which agrees with the mean clump separation caused by 'sausage instability' on a large scale. Our comprehensive CO line survey toward W 37 confirms the discovery of G 18.0–16.8 by Ragan et al. (2014), and identifies another GMF, G 16.5–15.8, lying $0.7°$ west of G 18.0–16.8. Both GMFs have very similar linear mass ratios of about $80 \, M_\odot$ pc^{-1},
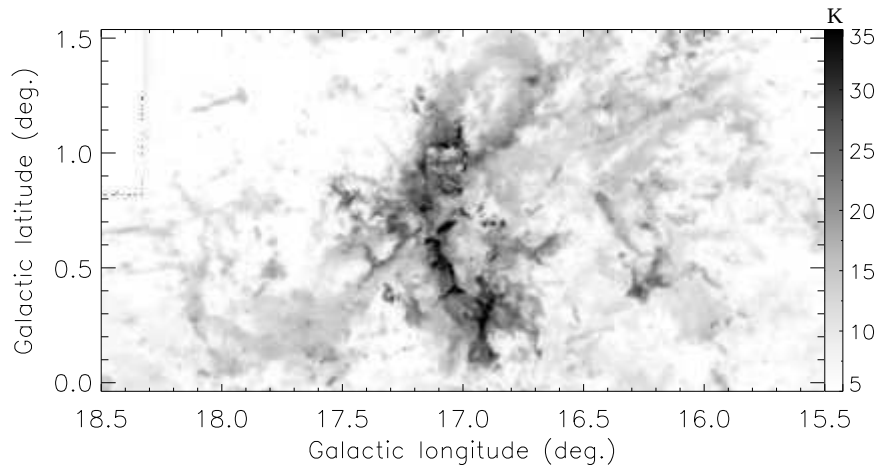
Fig. 7 Gas excitation temperature map of the observed region, derived from the radiation temperature of ^{12}CO $1-0$ emission in the range $16-27\,\mathrm{km\,s^{-1}}$.
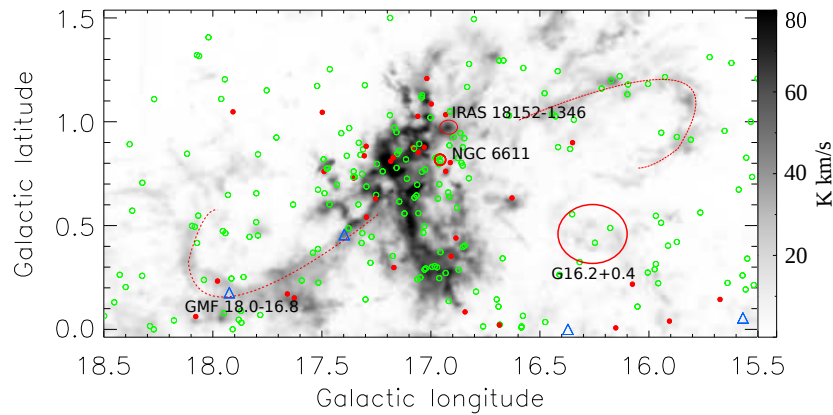

Fig. 8 The distribution of YSO candidates projected inside the observed region. The red circles represent class I objects, green circles are for class II objects, and blue triangles are for transition disk objects. The two GMFs are outlined by the red dashed lines. The locations of the high-mass young cluster NGC 6611, IRAS 18152–1346 and isolated molecular cloud G16.2+0.4 are denoted by the red circles/ellipses. The background is the integrated intensity map of ^{12}CO $1-0$.

far less than the maximum value of $300\,M_\odot\,\mathrm{pc^{-1}}$, over which a filament will break up into pieces. The gas excitation temperature map shows that W 37's dense ridge and northwestern part have higher temperatures than the ambient gas, in contrast with the dust temperature derived by Hill et al. (2012). Combining the spatial distributions of class I objects identified by the AllWISE catalog and the dense clumps from our CO emission maps, it is likely that the star formation activities within the northwestern part of W 37 are triggered by the associated nearby massive young cluster NGC 6611.

References

Alecian, E., Wade, G. A., Catala, C., et al. 2008, A&A, 481, L99
Castets, A., & Langer, W. D. 1995, A&A, 294, 835
Dame, T. M., Hartmann, D., & Thaddeus, P. 2001, ApJ, 547, 792
Elmegreen, B. G. 1998, in Astronomical Society of the Pacific Conference Series, 148, Origins, eds. C. E. Woodward, J. M. Shull, & H. A. Thronson, Jr., 150
Evans, C. J., Smartt, S. J., Lee, J.-K., et al. 2005, A&A, 437, 467
Guarcello, M. G., Prisinzano, L., Micela, G., et al. 2007, A&A, 462, 245

Guilloteau, S., & Lucas, R. 2000, in Astronomical Society of the Pacific Conference Series, 217, Imaging at Radio through Submillimeter Wavelengths, ed. J. G. Mangum & S. J. E. Radford, 299

Hill, T., Motte, F., Didelon, P., et al. 2012, A&A, 542, A114

Hillenbrand, L. A., Massey, P., Strom, S. E., & Merrill, K. M. 1993, AJ, 106, 1906

Indebetouw, R., Robitaille, T. P., Whitney, B. A., et al. 2007, ApJ, 666, 321

Koenig, X. P., & Leisawitz, D. T. 2014, ApJ, 791, 131

Koenig, R., & Smolin, J. A. 2014, Journal of Mathematical Physics, 55, 122202

Linsky, J. L., Gagné, M., Mytyk, A., McCaughrean, M., & Andersen, M. 2007, ApJ, 654, 347

Mannheim, P. D., & O'Brien, J. G. 2012, Phys. Rev. D, 85, 124020

Martayan, C., Floquet, M., Hubert, A. M., et al. 2008, A&A, 489, 459

McLeod, A. F., Dale, J. E., Ginsburg, A., et al. 2015, MNRAS, 450, 1057

Murray, N. 2011, ApJ, 729, 133

Penzias, A. A., & Burrus, C. A. 1973, ARA&A, 11, 51

Pound, M. W. 1998, ApJ, 493, L113

Ragan, S. E., Henning, T., Tackenberg, J., et al. 2014, A&A, 568, A73

Shan, W., Yang, J., Shi, S., et al. 2012, IEEE Transactions on Terahertz Science and Technology, 2, 593

Su, Y., Zhang, S., Shao, X., & Yang, J. 2015, ApJ, 811, 134

Sun, Y., Xu, Y., Yang, J., et al. 2015, ApJ, 798, L27

Vallée, J. P. 2008, AJ, 135, 1301

Wang, K., Testi, L., Ginsburg, A., et al. 2015, MNRAS, 450, 4043

Wright, E. L., Eisenhardt, P. R. M., Mainzer, A. K., et al. 2010, AJ, 140, 1868

Zuo, Y.-X., Li, Y., Sun, J.-X., et al. 2011, Chinese Astronomy and Astrophysics, 35, 439